JGR Solid Earth

RESEARCH ARTICLE
10.1029/2019JB017704

Effect of Fe^{3+} on Phase Relations in the Lower Mantle: Implications for Redox Melting in Stagnant Slabs

Ryosuke Sinmyo[1,2], Yoichi Nakajima[1], Catherine A. McCammon[1], Nobuyoshi Miyajima[1], Sylvain Petitgirard[1], Robert Myhill[1], Leonid Dubrovinsky[1], and Daniel J. Frost[1]

[1]Bayerisches Geoinstitut, Universitaet Bayreuth, Bayreuth, Germany, [2]Department of Physics, School of Science and Technology, Meiji University, Kanagawa, Japan

Key Points:
- We determined phase relationships of Fe3+-rich system at top of the lower mantle
- Melting temperature of Fe3+-rich system is lower than Fe2+-dominant system
- Fe3+ may not be transported into the deep lower mantle because of its incompatibility

Supporting Information:
- Supporting Information S1

Correspondence to:
R. Sinmyo,
sinmyo@meiji.ac.jp

Citation:
Sinmyo, R., Nakajima, Y., McCammon, C. A., Miyajima, N., Petitgirard, S., Myhill, R., et al. (2019). Effect of Fe^{3+} on phase relations in the lower mantle: Implications for redox melting in stagnant slabs. *Journal of Geophysical Research: Solid Earth*, *124*, 12,484–12,497. https://doi.org/10.1029/2019JB017704

Received 18 MAR 2019
Accepted 17 OCT 2019
Accepted article online 21 OCT 2019
Published online 4 DEC 2019

The copyright line for this article was changed on 11 MAR 2020 after original online publication.

Abstract Recent studies have revealed that Earth's deep mantle may have a wider range of oxygen fugacities than previously thought. Such a large heterogeneity might be caused by material subducted into the deep mantle. However, high-pressure phase relations are poorly known in systems including Fe^{3+} at the top of the lower mantle, where the subducted slab may be stagnant. We therefore conducted high-pressure and high-temperature experiments using a multi-anvil apparatus to study the phase relations in a Fe^{3+}-bearing system at 26 GPa and 1573–2073 K, at conditions prevailing at the top of the lower mantle. At temperatures below 1923 K, $MgSiO_3$-rich bridgmanite, an Fe^{3+}-rich oxide phase, and SiO_2 coexist in the recovered sample. Quenched partial melt was observed above 1973 K, which is significantly lower than the solidus temperature of an equivalent Fe^{3+}-free bulk composition. The partial melt obtained from the Fe^{3+}-rich bulk composition has a higher iron content than coexisting bridgmanite, similar to the Fe^{2+}-dominant system. The results suggest that strong mantle oxygen fugacity anomalies might alter the subsolidus and melting phase relations under lower mantle conditions. We conclude that (1) a small amount of melt may be generated from an Al-depleted region of a stagnant slab, such as subducted former banded-iron-formation, and (2) Fe^{3+} is not transported into the deep part of the lower mantle because of its incompatibility during melting.

1. Introduction

1.1. Phase Relations in the Lower Mantle

The Earth's lower mantle is mainly composed of $(Mg,Fe)SiO_3$-rich bridgmanite and (Mg,Fe)O ferropericlase (Frost & Myhill, 2016; Ito & Takahashi, 1989). Because the lower mantle is the most voluminous reservoir on Earth, it is important to understand the phase relations and physical properties of lower mantle minerals in order to constrain the structure and the evolution of Earth's interior. The subsolidus phase relations (Fei et al., 1991, 2004; Ishii, Huang, et al., 2018; Ito & Takahashi, 1989) and melting phase relations under lower mantle conditions have been widely studied, mostly in the simple $MgO\text{-}Fe^{2+}O\text{-}SiO_2$ system, to understand the chemical evolution during geological events such as the solidification of the magma ocean (Boukare et al., 2015; Ito et al., 2004; Liebske & Frost, 2012; Nomura et al., 2011). However, phase relations in systems including Fe^{3+} under lower mantle conditions are poorly known, although as detailed below a high valence state of iron has been reported in recent observations and laboratory experiments.

1.2. Oxidation State of Natural Samples From the Deep Mantle

Recent analyses of natural samples have revealed that the Earth's deep mantle may have a wide range of oxygen fugacities (Kagi et al., 2016; Kaminsky et al., 2015; Kiseeva et al., 2018; Smith et al., 2016; Stagno et al., 2013; Wirth et al., 2014). Studies of peridotites have shown that the oxygen fugacity generally decreases with increasing depth to ~200 km, from the QFM (quartz-fayalite-magnetite) buffer to three log units below QFM (Stagno et al., 2013). In contrast, inclusions in diamonds from depths of >200 km contain considerable amounts of Fe^{3+} (Kaminsky et al., 2015; Kiseeva et al., 2018; Wirth et al., 2014), Fe^0 (Kagi et al., 2016; Smith et al., 2016), and Fe^{2+}. This may reflect the wide range of oxygen fugacities and the disproportionation reaction of iron in high-pressure minerals such as garnet and bridgmanite (Frost et al., 2004; Rohrbach et al., 2007; Smith et al., 2016). Kaminsky et al. (2015) estimated that diamond inclusions derived from the lower mantle have a high oxygen fugacity around the QFM buffer. This oxygen fugacity is as high as that of Mid-

ocean ridge basalt glass samples (Frost & McCammon, 2008), in contrast to relatively reduced (around three log units below QFM) peridotite at ~200-km depth (Stagno et al., 2013). Because the formation of such ultra-deep diamonds is likely related to subducted material at the top of the lower mantle (Smith et al., 2016), the high redox state of the inclusions strongly suggests that the oxygen fugacity of stagnant slabs at the top of the lower mantle varies widely. Recently, Kiseeva et al. (2018) suggested that highly oxidized minerals in diamond inclusions may be influenced by carbonaceous melt or fluid. Indeed, fluid inclusions with a wide variety of redox states, containing compounds such as H_2, H_2O, and CH_4, have been found in diamond from the deep mantle (Smith et al., 2016; Tschauner et al., 2018). It is suggested that sedimentary banded-iron-formations (BIF) may be transported into the deep mantle by subduction (Dobson & Brodholt, 2005; Kang & Schmidt, 2017). The subducted BIFs, which are Fe^{3+} rich and almost Al free, may supply highly oxidized material to the deep mantle (Kang & Schmidt, 2017).

1.3. Fe^{3+} in Lower Mantle Minerals

In contrast to other mantle minerals, bridgmanite can accommodate a large amount of Fe^{3+} (Frost & McCammon, 2008). It is known that Fe^{3+} has a strong effect on the elasticity, element partitioning, and transport properties of bridgmanite (Gu et al., 2016; Kurnosov et al., 2017; Piet et al., 2016; Shim et al., 2017; Sinmyo, Pesce, et al., 2014). For instance, recent experimental studies have shown that the seismic wave velocity of the upper part of the lower mantle can be explained by the strong effect of Fe^{3+} on the sound wave velocity of bridgmanite (Kurnosov et al., 2017). It is known that Fe^{3+} is quite stable in Al-bearing bridgmanite; metallic iron is formed via the following disproportionation reaction: $2Fe^{2+} = Fe^{3+} + Fe^0$ (Frost et al., 2004). Although this can be interpreted by a stable coupled substitution mechanism of $Al^{3+} + Fe^{3+} = Mg^{2+} + Si^{4+}$ in bridgmanite, several studies have reported that bridgmanite can also contain a moderate amount of Fe^{3+}, even in the Al-free system (Andrault & Bolfan-Casanova, 2001; Hummer & Fei, 2012). Based on its large unit cell volume, natural bridgmanite in the Tenham meteorite likely contains a large amount of Fe^{3+} without aluminum (Tschauner et al., 2014).

The phase relations of deep mantle minerals in the Fe^{3+}-bearing system are not well understood because of measurement challenges in determination of Fe^{3+}/total Fe ratio. Pioneering work using a laser-heated diamond anvil cell at ~20 GPa and 2500 K revealed the stability of a distorted spinel-like phase with chemical composition between $MgFe_2O_4$ and Mg_2SiO_4 (Andrault & Bolfan-Casanova, 2001). The effect of Fe^{3+} on subsolidus phase relations has been studied under conditions of the transition zone and lower mantle, mostly using multi-anvil experiments (Frost & McCammon, 2009). On the other hand, several new phases with a wide stoichiometry range were found in the Fe-O system under high-pressure conditions, including FeO_2, Fe_4O_5, Fe_5O_6, Fe_7O_9, Fe_9O_{11}, Fe_5O_7, $Fe_{13}O_{19}$, and $Fe_{25}O_{32}$ (Bykova et al., 2016; Hu et al., 2016; Ishii, Uenver-Thiele, et al., 2018; Lavina et al., 2011; Lavina & Meng, 2015; Merlini et al., 2015; Sinmyo et al., 2016), in addition to common FeO, Fe_3O_4, and Fe_2O_3. Accordingly, the phase relations are being intensively studied to understand the effect of such newly identified iron oxides on mantle phase relations (Myhill et al., 2016; Uenver-Thiele et al., 2017).

1.4. Melting at the Top of the Lower Mantle?

Observations and theory indicate that partial melt may be present above and below the transition zone (Hirschmann, 2006). For instance, a low-velocity seismic wave anomaly was observed beneath North America (Schmandt et al., 2014), where the Farallon slab may be stagnant at ~660-km depth (Schmid et al., 2002). Schmandt et al. (2014) suggested that such a low-velocity zone can be attributed to partial melting due to the dehydration of hydrous ringwoodite (Pearson et al., 2014), although the hydrous transition zone model remains controversial (Kelbert et al., 2009; Yoshino et al., 2008). Liu et al. (2018) reported a low-velocity zone atop the 410-km discontinuity and in the upper part of the lower mantle (~800-km depth) beneath the European Alps. Freitas et al. (2017) showed that the global low-velocity layer atop the 410-km discontinuity can be explained by the reduction of velocity due to partial melting. The solidus of mantle rocks has been repeatedly studied under such deep-mantle conditions, in both an anhydrous system (Ito et al., 2004; Trønnes & Frost, 2002) and in H_2O- and CO_2-present systems (Dasgupta & Hirschmann, 2006; Litasov et al., 2014). However, the effect of oxygen fugacity on melting temperature under lower mantle conditions remains poorly understood.

We conducted high-pressure and high-temperature experiments using a multi-anvil apparatus to study the effect of Fe^{3+} on phase relations under lower mantle conditions. The results show that the solidus temperature of the Fe^{3+}-bearing system is significantly lower than that of the Fe^{3+}-free bulk composition. This implies that strong anomalies in mantle oxygen fugacity affect the melting and subsolidus phase relations of the lower mantle.

2. Experiments

2.1. Starting Material and High-P–T Experiments

MgO, SiO_2, and Fe_2O_3 (95% enriched in ^{57}Fe) were ground together for 1 h in a silicon nitride mortar with acetone and then dehydrated at 1273 K for several hours in air before use. MgO was dried at 1273 K for several hours just before weighing. After mixing by mortar, the obtained oxide mixture was dried again at 1273 K. ^{57}Fe was enriched for Mössbauer spectroscopy measurements. The purities of the starting materials are reagent grade (purity >99.9%). Starting material with the following stoichiometry was prepared: $Mg_{0.95}Fe_{0.10}Si_{0.95}O_3$ and $Mg_{0.75}Fe_{0.50}Si_{0.75}O_3$, which simulates the addition of an Fe_2O_3 component in $MgSiO_3$. A Kawai-type multi-anvil press was used to generate high pressures and temperatures (Keppler & Frost, 2005). All experimental runs were conducted at ~26 GPa, corresponding to the pressure at the top of the lower mantle. The high-pressure experiments were performed using a pressure medium of MgO + 5 wt % Cr_2O_3 octahedron with edge length of 7 mm and tungsten carbide anvils with a truncated edge length of 3 mm. Pressure calibrations are shown in Keppler and Frost (2005). A $LaCrO_3$ heater was used, and the temperatures were monitored with a W3%Re–W25%Re thermocouple. All ceramics used in the pressure cell assembly were dried at 1273 K before sample loading. The sample was loaded into gold or platinum capsules and inserted into an MgO container. The multichamber capsule method was used for run #17 (Liebske & Frost, 2012). A cylindrical platinum rod with holes was used as a capsule, which helps to ensure similar sample conditions. After inserting the sample container into the pressure medium, the cell assembly was kept in an oven at 393 K until the experiment. After compression to the desired pressure, we increased the temperature at about +100 K/min. The experimental conditions are summarized in Table 1.

2.2. Analysis of Recovered Samples

The recovered samples were examined using an electron microprobe (JEOL JXA-8200) at Bayerisches Geoinstitut (BGI) and a field emission scanning electron microscope, also at BGI (Field-Emission-Type Scanning Electron Microscope; Leo Gemini 1530). Typical Field-Emission-Type Scanning Electron Microscope images are shown in Figure 1. The chemical composition of the samples was determined using an electron microprobe operated at 15 kV and 15 nA with standards of pure iron metal for Fe, and forsterite for Si and Mg. The acquisition times for the peak and background of each element were 20–30 and 10–15 s, respectively. A focused beam was used for the analysis of crystalline samples, whereas a broad defocused beam with a diameter of 10–20 μm was used to obtain the average composition of quenched melt portions.

Selected samples were removed from the capsule and crushed into several pieces for powder X-ray diffraction (XRD) measurements using a FR-D high-brilliance Rigaku diffractometer at BGI with Mo Kα radiation operated at 55 kV and 60 mA (Figure 2). Fine pure silicon powder was used as a calibration standard. In addition, we conducted Mössbauer spectroscopy with a nominal ^{57}Co high specific activity source in a rhodium matrix at BGI (Figure 3). For Mössbauer spectroscopy, the bridgmanite crystals were removed from the thin section prepared for scanning electron microscope analysis and compacted into a flat pellet. The Mössbauer spectra were analyzed using the MossA software package (Prescher et al., 2012). To better constrain the redox state of the liquid, we extracted a thin section from the quenched liquid texture in sample #16 using a focused ion beam system (FEI Scios DualBeam) at BGI and thinned it for electron transparency down to ~50 nm. The lamella was then further analyzed using a transmission electron microscope (PHILIPS CM20 FEG) operated at 200 kV and equipped with electron energy loss spectroscopy (EELS; Gatan PEELS 666). A typical image is shown in Figure 4. Our full suite of measurements show that the Fe^{3+}/total Fe ratio remains high in the recovered sample as expected. Mössbauer spectroscopy is a well-established method in the determination of the Fe^{3+}/total Fe ratio and complements EELS and the flank method by microprobe analysis (Lauterbach et al., 2000; Longo et al., 2011). Fourier-transform infrared spectroscopy measurements on a recovered sample showed that the sample was almost anhydrous (Figure S1 in the supporting

Table 1
Experimental Conditions

Run #	Temperature (K)	Starting material	Duration (min)	Capsule materials	Phases[a]
#04 (S5198)	1673[b]	$Mg_{0.95}Fe_{0.10}Si_{0.95}O_3$	45	Gold	Bdg, Fe-rich oxide phase
#07 (S5644)	1973	$Mg_{0.95}Fe_{0.10}Si_{0.95}O_3$	45	Gold	Bdg, liquid
#08 (S5644)	1973	$Mg_{0.75}Fe_{0.50}Si_{0.75}O_3$	45	Gold	Bdg, St, liquid
#09 (S5649)[c]	1573	$Mg_{0.75}Fe_{0.50}Si_{0.75}O_3$	1	Gold	Bdg, St, Fe-rich oxide phase
#14 (S5789)	1873	$Mg_{0.75}Fe_{0.50}Si_{0.75}O_3$	60	Gold	Bdg, St, Fe-rich oxide phase
#16 (S5960)	2073	$Mg_{0.75}Fe_{0.50}Si_{0.75}O_3$	20	Platinum	Bdg, St, liquid
#17-1 (S5967)	1923	$Mg_{0.75}Fe_{0.50}Si_{0.75}O_3$	30	Platinum	Bdg, St, Fe-rich oxide phase
#17-2 (S5967)	1923	$Mg_{0.95}Fe_{0.10}Si_{0.95}O_3$	30	Platinum	Bdg
#17-3 (S5967)	1923	$Mg_{0.75}Fe_{0.50}Si_{0.75}O_3$	30	Platinum	Bdg, St, Fe-rich oxide phase

[a]Bdg, $MgSiO_3$-rich bridgmanite; St, SiO_2 stishovite. [b]Estimated from electrical power. [c]The sample may not be in equilibrium because of the short heating duration.

information), as the multi-anvil experiments have been prepared in the same manner with previous studies on silicate melting relations in anhydrous system (e.g., Liebske & Frost, 2012; Trønnes & Frost, 2002).

3. Results

3.1. Sample Characterization

Bridgmanite, stishovite, and an Fe^{3+}-rich phase were observed in the samples recovered from temperatures below 1923 K (Tables 1 and 2). The results of Mössbauer spectroscopy show that iron in bridgmanite is mostly Fe^{3+} (Fe^{3+}/total Fe = 0.6–0.8). The hyperfine parameters of bridgmanite are consistent with those of previous studies (Sinmyo et al., 2017). Unfortunately, we could not obtain the Fe^{3+}/total Fe ratio of iron oxide by Mössbauer spectroscopy because of the limited sample amount (Figure 1). On the other hand, we observed crystals of Fe_4O_5 in the quenched melt of run #16 by sample characterization using transmission electron microscope (Figure 4). The obtained electron diffraction pattern is consistent with that of a previous study (Myhill et al., 2016). The EELS spectra show a broad Fe $L_{2,3}$-edge, which may be due to electron charge transfer between Fe^{2+} and Fe^{3+} (Ovsyannikov et al., 2016). Although it is not straightforward to obtain the Fe^{3+}/total Fe ratio because of the broadness, the sample spectra indicate a high Fe^{3+}/total Fe ratio (van Aken et al., 1998). The Fe^{3+}/total Fe ratio of the iron oxides was estimated based on the stoichiometry (Table 1). Based on the results of run #17 and that of a previous study using the same cell assemblage, we estimated the bulk Fe^{3+}/total Fe ratios of the run products of $Mg_{0.95}Fe_{0.10}Si_{0.95}O_3$ and $Mg_{0.75}Fe_{0.50}Si_{0.75}O_3$ to be 0.6 and 0.8, respectively (Sinmyo et al., 2016). The Fe^{3+}/total Fe ratios and hyperfine parameters of bridgmanite are summarized in Tables 2 and 3. The unit cell parameters of our bridgmanite sample were obtained from XRD measurements (Table 2) and gave much higher values compared to those of $(Mg,Fe^{2+})SiO_3$ bridgmanite (Figure 5).

3.2. Chemical Analysis and Phase Relations

The results of the chemical analysis are summarized in Table 2. At temperatures below 1923 K, we observed $MgSiO_3$-rich bridgmanite, an iron-rich oxide phase, and stishovite in the recovered sample using XRD measurements and microprobe analysis. Bridgmanite and iron oxide contain 4–6 and 73–84 wt % FeO* (total iron as $Fe^{2+}O$), respectively. Although we observed high-pressure minerals in the recovered sample from run #09, the sample may not be in equilibrium due to the short heating duration. At temperatures above 1973 K, quenched melt, bridgmanite, and stishovite were observed in the sample (Figure 1). The microprobe analysis results show that bridgmanite and melt contain 4–17 and 33–44 wt % FeO*, respectively. Table 2 and Figure 6 summarize the chemical compositions of the phases. While Fe^{3+}/total Fe ratios of bridgmanite were estimated by Mössbauer spectroscopy (Table 2), the chemical compositions of melt were calculated assuming Fe^{3+}/total Fe ratio = 0.5–1 (Figure 6). This is because it is not straightforward to determine the Fe^{3+} ratio in the melt, unfortunately. Fe^{3+}/total Fe ratios of the iron oxides were estimated based on the stoichiometry as discussed below. Stishovite is almost pure SiO_2 in all recovered samples. The total values of the iron oxide and liquid phases are significantly lower than 100% (Table 2) because of the assumed valence state of iron and the surface roughness. The low values in iron oxide can be explained by the Fe^{3+} content, as

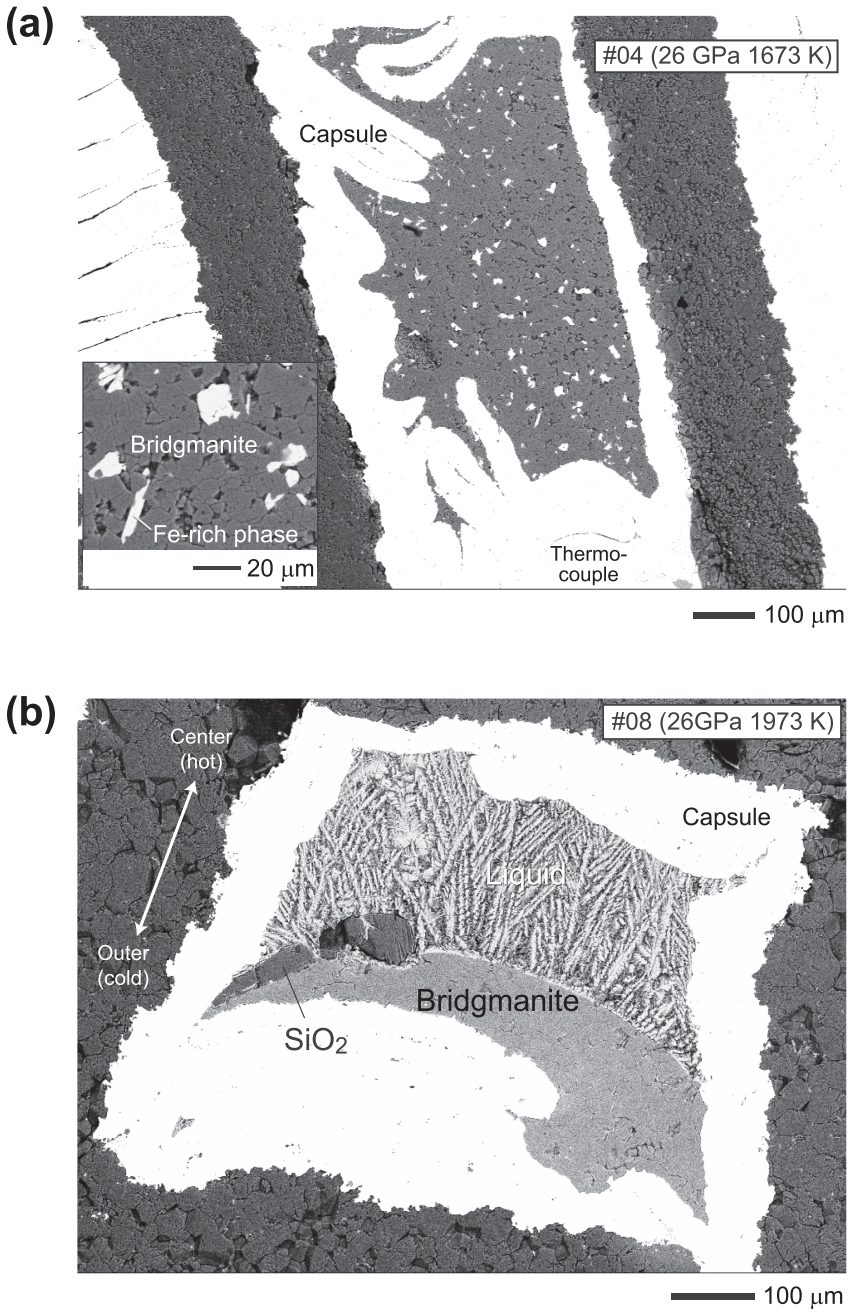

Figure 1. Backscattered electron images of the recovered samples synthesized at 26 GPa and (a) 1673 K and (b) 1973 K.

discussed below. The low total value in liquid may be due to the rough surface including submicron quench crystals. The chemical composition of the liquid was normalized to 100%.

The obtained results indicate that Fe^{3+}-rich iron oxide, bridgmanite, and stishovite are stable below 1923 K (Table 2 and Figure 6a). No chemical zoning was observed in the backscattered electron images of the phases (Figure 1). Although bridgmanite and stishovite are almost stoichiometric, Fe^{3+}-rich iron oxide is not. For example, the composition of iron oxide in run #04 is 73.3 wt% FeO* and 16.2 wt% MgO (Table 2), which can be written as $(Mg_{0.84}Fe^{2+}_{0.19})Fe^{3+}_{1.94}O_4$ and $(Mg_{0.56}Fe^{2+}_{0.36})_2Fe^{3+}_{2.05}O_5$ if we assume that Fe^{3+}/total Fe of iron oxides are 0.91 and 0.68, respectively. Although these chemical formulae do not perfectly match $(Mg,Fe^{2+})Fe^{3+}{}_2O_4$ and $(Mg,Fe^{2+})_2Fe^{3+}{}_2O_5$ stoichiometry, the iron oxide in run #04 is most likely $(Mg,Fe^{2}$

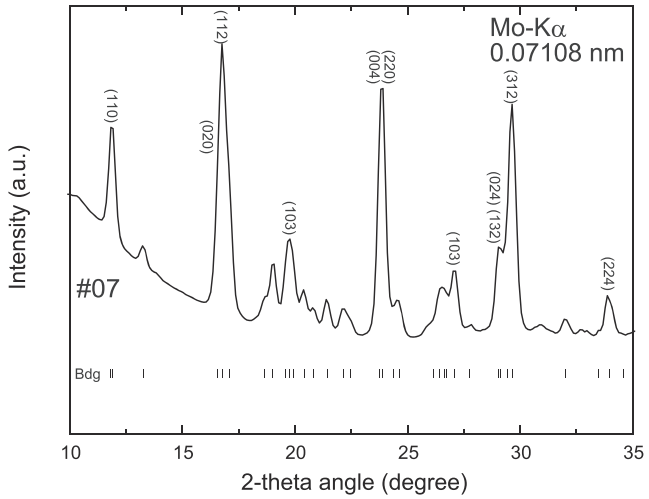

Figure 2. Powder XRD pattern of run #07. The vertical lines are the 2-theta values expected for diffraction peaks of bridgmanite. Mirror indexes are shown for major peaks.

$^{+})_2Fe^{3+}{}_2O_5$ because the bulk Fe^{3+}/total Fe ratio is ~ 0.6, as discussed above. Similarly, the Fe^{3+}/total Fe values of runs #09, #14, and #17 were estimated assuming $(Mg,Fe^{2+})Fe^{3+}{}_2O_4$ stoichiometry to reconcile the bulk Fe^{3+}/total Fe ratio of ~ 0.8 (Table 2). While the Fe^{3+}/total Fe ratio of iron oxide is somewhat uncertain, the iron oxide is not likely to occur as (Mg,Fe)O magnesiowüstite because the exchange partition coefficient of iron between bridgmanite and magnesiowüstite, $K_{FeO^*}^{Bdg/Fp} = \left(X_{FeO^*}^{Bdg}/X_{MgO}^{Bdg}\right)/(X_{FeO^*}^{Fp}/X_{MgO}^{Fp})$, is reported to be moderate ($K_{FeO^*}^{Bdg/Fp}$ ~ 0.1–0.4) (Nakajima et al., 2012) compared to the current case ($K_{FeO^*}^{Bdg/Oxide}$ ~ 0.02).

It is known that iron in the sample can be partly lost into platinum (Rubie et al., 1993). However, the solubility of iron in platinum is limited at high oxygen fugacity and diffusion is very slow. According to a previous study (Rubie et al., 1993), 1 wt % of iron diffuses into platinum about 10 μm from a silicate sample heated at 1673 K for 360 min, which are comparable heating conditions to our experiments (Table 1). Since the sample is larger than the diffusion length (Figure 1), we expect that only a negligible amount of iron should be lost into the platinum capsule under the experimental conditions used. Indeed, a mass balance calculation showed that the bulk iron content in the recovered sample is consistent with the starting material.

4. Discussion

4.1. The Possible Effect of the Water in the Sample

Generally, the solidus is much lower in the H_2O-bearing system compared to the equivalent anhydrous system. While our results showed that the solidus was significantly lower than that of previous studies in the anhydrous Fe^{2+}-dominant system, lower solidus may not be because of water. Because the experiments have been prepared in the same manner as previous studies on the melting relationsin the anhydrous silicate system (e.g., (Liebske & Frost, 2012; Trønnes & Frost, 2002)). The samples wereconfirmed to be anhydrous in those previous studies. Moreover, we did not observe any additional phase other than bridgmanite in run #17-2 (Table 1). If the sample was hydrous, the recovered sample in run #17-2 should contain hydrous minerals, since the bridgmanite can hardly accommodate water (Bolfan-Casanova et al., 2000; Bolfan-Casanova et al., 2003; Inoue et al., 2010). Also, obtained Fourier-transform infrared spectroscopy spectra showed that the recovered sample was almost anhydrous (Figure S1), although it may not prove that the samples were anhydrous during experiments.

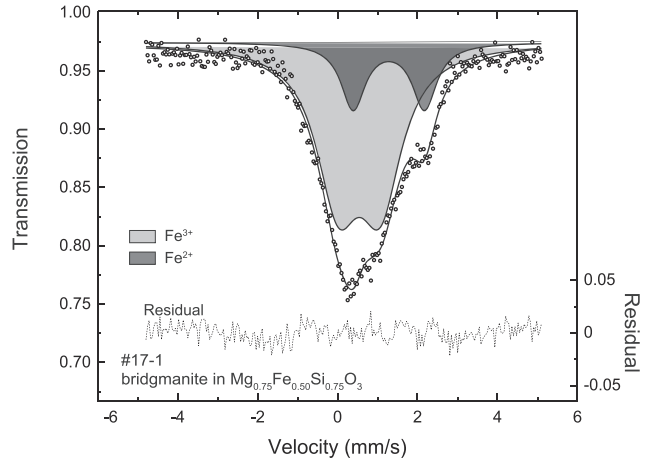

Figure 3. Typical Mössbauer spectrum, measured at room temperature on the sample recovered from run #17-1.

4.2. Mineral Chemistry of Fe^{3+}-Bearing Bridgmanite

The lattice volume of Fe^{3+}-bearing bridgmanite is significantly larger than that of pure $MgSiO_3$ and $(Mg,Fe^{2+})SiO_3$ (Figure 5). This is consistent with previous studies on Al-free, Fe^{3+}-bearing bridgmanite (Hummer & Fei, 2012; Sinmyo, Bykova, et al., 2014). In addition, the obtained volume is similar to that of natural Al-free bridgmanite found in a shock vein within natural meteorites (Tschauner et al., 2014). Because the shock vein also contains $(Mg,Fe)SiO_3$ glass likely former liquid, bridgmanite may be able to accommodate a large amount of Fe^{3+}, even under high-temperature conditions close to the melting point. It is shown that the unit cell volume of bridgmanite increases with increasing amount of Fe^{3+} and is likely independent of Al content (Figure 5). This may be related to tilting of octahedra in the Pbnm perovskite-type crystal structure (Sinmyo, Bykova, et al., 2014).

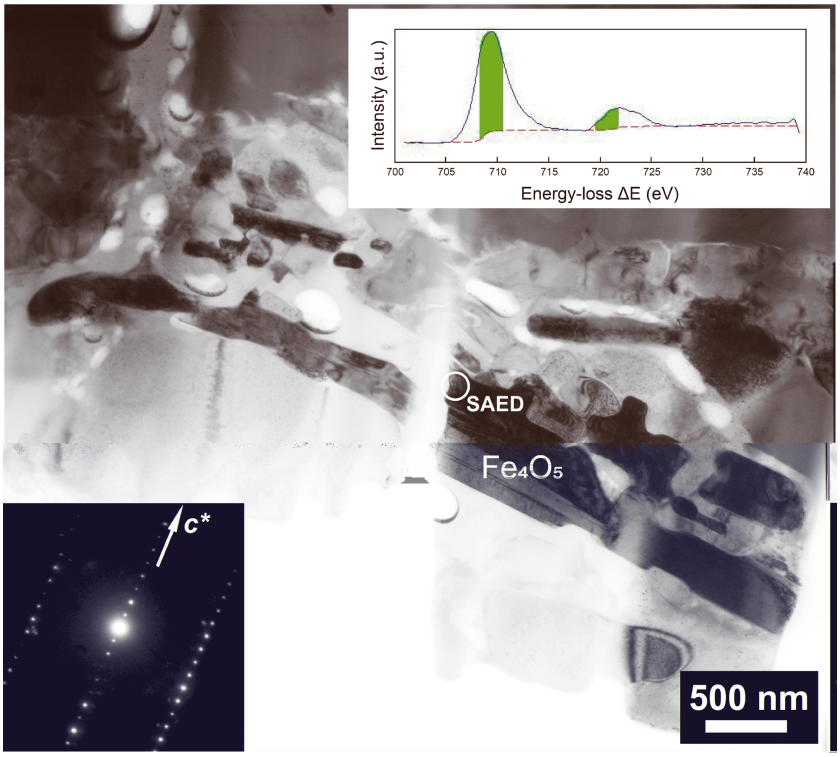

Figure 4. TEM image of the recovered sample and selected area electron diffraction pattern of Fe_4O_5 (lower left) in quenched melt of run #16. The inset (upper right) is the Fe $L_{2,3}$-energy loss near edge structure (ELNES) of the Fe_4O_5 phase. Green areas are integrated window for the determination of the Fe^{3+}/Fe total ratio (van Aken et al., 1998).

We compared the Si and Fe^{3+} concentrations to identify the Fe^{3+} substitution mechanism in bridgmanite (Figure 5). Four possible substitution mechanisms are considered:

$$Fe_2O_3 + {}^{[A]}Mg^{\times} + {}^{[B]}Si^{\times} \leftrightarrow MgO + SiO_2 + {}^{[A]}Fe + {}^{[B]}Fe' \quad (1)$$

$$Fe_2O_3 + 2{}^{[B]}Si^{\times} + {}^{[O]}O^{\times} \leftrightarrow 2SiO_2 + 2{}^{[B]}Fe' + {}^{[O]}V^{\cdot\cdot} \quad (2)$$

$$Fe_2O_3 + 3{}^{[A]}Mg^{\times} + 3{}^{[B]}Si^{\times} \leftrightarrow 3MgO + 2{}^{[A]}Fe^{\cdot} + {}^{[A]}V'' + 3{}^{[B]}Si^{\times} \quad (3)$$

$$2Fe_2O_3 + 4{}^{[A]}Mg^{\times} + 4{}^{[B]}Si^{\times} \leftrightarrow 4MgO + SiO_2 + 4{}^{[A]}Fe^{\cdot} + {}^{[B]}V'''' + 3{}^{[B]}Si^{\times}, \quad (4)$$

where the superscript symbols $^{\times}$, $^{\cdot}$, and $'$ indicate neutral, positive, and negative charges, respectively (Kröger & Vink, 1956), and V indicates a vacancy. The brackets [A], [B], and [O] show the crystallographic site of the ABO_3 perovskite-type structure. The number of the symbols in superscript indicates the number of charges. The substitution mechanism changes with increasing Fe^{3+} concentration (Figure 7). The coupled substitution mechanism shown in equation 1 may be dominant below ~0.08 Fe^{3+} per formula unit (pfu). This is consistent with a previous study by Hummer and Fei (2012), although they found the value to be below <0.07 pfu. At ~0.2 Fe^{3+} pfu, Fe^{3+} is substituted into the A site, creating a vacancy at the B site, as shown in equation 4. This is consistent with our previous studies using single-crystal XRD measurements and Mössbauer spectroscopy (Sinmyo, Bykova, et al., 2014; Sinmyo et al., 2017). However, we cannot exclude the possible occurrence of other substitution mechanism, such as (1) and (2) based on the limited XRD data. The maximum solubility of Fe^{3+} in bridgmanite increases with increasing temperature (Figure 6). This may explain why the substitution of a large amount of Fe^{3+} is associated with the formation of vacancies in the crystals. In general, the number of defects in the crystal structure increases with increasing temperature (Siegel, 1978). Indeed, it was recently shown that the oxygen vacancy content in the bridgmanite structure increases with temperature (Liu et al., 2019). Our experimental results suggest that incorporation of Fe^{3+} may

Table 2
Results of Chemical Analysis

	N	SiO_2 (wt %)	FeO[*a]	MgO	Total	Proportions[b]	Fe^{3+}/total Fe	Unit cell volume (Å^3)
#04 (S5198), 1673 K, $Mg_{0.95}Fe_{0.10}Si_{0.95}O_3$								
Bridgmanite	22	58.7(8)	4.2(5)	38.2(6)	101.1(8)	0.96	-	
Fe^{3+}-rich phase	11	0.80(8)	73.3(73)	16.2(16)	90.3(90)	0.04	0.68[c]	
#07 (S5644), 1973 K, $Mg_{0.95}Fe_{0.10}Si_{0.95}O_3$								
Bridgmanite	20	57.8(7)	4.7(3)	38.8(5)	101.3(9)	0.95	0.57(5)[d]	163.4(3)
Liquid	2	17.3(7)	44.0(4)	38.7(2)	100(4)	0.05	-	
#08 (S5644), 1973 K, $Mg_{0.75}Fe_{0.50}Si_{0.75}O_3$								
Bridgmanite	22	50.0(13)	16.1(11)	32.7(9)	98.8(13)	0.04	-	167.0(4)
Liquid	20	40.1(7)	32.9(8)	27.0(8)	100(4)	0.96	-	
St	2	100.5(5)	0.5(1)	0.0(0)	101.0(5)	0.00	-	
#09 (S5649), 1573 K, $Mg_{0.75}Fe_{0.50}Si_{0.75}O_3$								
Bridgmanite	7	57.4(7)	6.3(6)	38.7(3)	102.4(4)	0.62	-	
Fe^{3+}-rich phase	10	1.6(9)	79.8(1.9)	10.9(9)	92.3(7)	0.33	0.80[f]	
St	3	95.5(4)	2.5(17)	0.3(4)	98.3(17)	0.06	-	
#14 (S5789), 1873 K, $Mg_{0.75}Fe_{0.50}Si_{0.75}O_3$								
Bridgmanite	20	53.5(7)	13.1(3)	32.9(8)	99.5(13)	0.75	-	
Fe^{3+}-rich phase	14	2.1(1)	82.6(7)	7.6(2)	92.3(7)	0.25	0.74[f]	
St (trace)[e]	20	89.8(26)	1.4(4)	3.0(20)	94.2(5)	0.00	-	
#16 (S5960), 2073 K, $Mg_{0.75}Fe_{0.50}Si_{0.75}O_3$								
Bridgmanite	19	47.7(16)	16.8(9)	29.2(15)	93.7(13)	0.13	0.74(5)[d]	165.7(3)
Liquid	20	46.2(30)	32.9(18)	20.9(21)	100(13)	0.87	-	
#17-1 (S5967), 1923 K, $Mg_{0.75}Fe_{0.50}Si_{0.75}O_3$								
Bridgmanite	15	52.1(7)	14.6(10)	32.7(7)	99.8(11)	0.76	0.80(5)[d]	164.4(6)
Fe^{3+}-rich phase	14	2.4(6)	83.6(6)	7.9(6)	93.9(9)	0.24	0.73[f]	
St (trace)[e]	2	96.6(14)	0.0(0)	0.0(0)	96.6(14)	0.00	-	
#17-2 (S5967), 1923 K, $Mg_{0.95}Fe_{0.10}Si_{0.95}O_3$								
Bridgmanite	15	58.1(7)	4.2(5)	39.2(9)	101.4(8)		0.60(5)[d]	163.3(4)
#17-3 (S5967), 1923 K, $Mg_{0.75}Fe_{0.50}Si_{0.75}O_3$								
Bridgmanite	13	52.5(6)	14.1(7)	33.1(6)	99.7(15)	0.76	-	
Fe^{3+}-rich phase	16	1.6(3)	81.3(8)	8.8(4)	91.7(11)	0.24	0.76[f]	
St (trace)[e]	2	91.2(4)	0.9(0)	0.6(5)	92.7(6)	0.00	-	

[a]Total iron as $Fe^{2+}O$. [b]Based on mass balance calculations. [c]Estimated value based on an assumption of $(Mg,Fe^{2+})_2Fe^{3+}{}_2O_5$ stoichiometry. [d]Based on Mössbauer spectroscopy. [e]Relatively low total values are likely due to the detections of other elements during measurements in tiny grain size. [f]Estimated value based on an assumption of $(Mg,Fe^{2+})Fe^{3+}{}_2O_4$ stoichiometry.

accompany the formation of defects in Fe^{3+}-rich bridgmanite (Figure 7). Although the substitution mechanism does not have a strong effect on the elastic properties, it can affect the electrical/thermal conductivity (Okuda et al., 2017; Yoshino et al., 2016). Conduction of charge carriers (electron, ion, and

Table 3
Hyperfine Parameters of Fe^{3+}-Rich Bridgmanite Determined From Mössbauer Spectra

Component	CS (mm/s)	FWHM (mm/s)	Area (%)	QS (mm/s)	Fe^{3+}/total Fe (%)[a]
#07					
Fe^{2+} (Bdg)	1.15(1)	0.65(4)	43.5(16)	1.74(2)	56.5(50)
Fe^{3+} (Bdg)	0.44(1)	0.73(3)	56.5(16)	0.88(2)	
#16					
Fe^{2+} (Bdg)	1.37(6)	0.70(25)	26.3(70)	1.81(11)	73.7(50)
Fe^{3+} (Bdg)	0.45(4)	0.92(13)	73.7(70)	0.97(7)	
#17-1					
Fe^{2+} (Bdg)	1.23(3)	0.74(12)	20.5(32)	1.77(6)	79.5(50)
Fe^{3+} (Bdg)	0.49(2)	1.29(9)	79.5(32)	1.04(4)	
#17-2					
Fe^{2+} (Bdg)	1.09(2)	0.60(5)	40.1(24)	1.74(3)	59.9(50)
Fe^{3+} (Bdg)	0.43(2)	0.78(6)	59.9(24)	0.86(3)	

[a]Uncertainty includes uncertainty of the model itself.

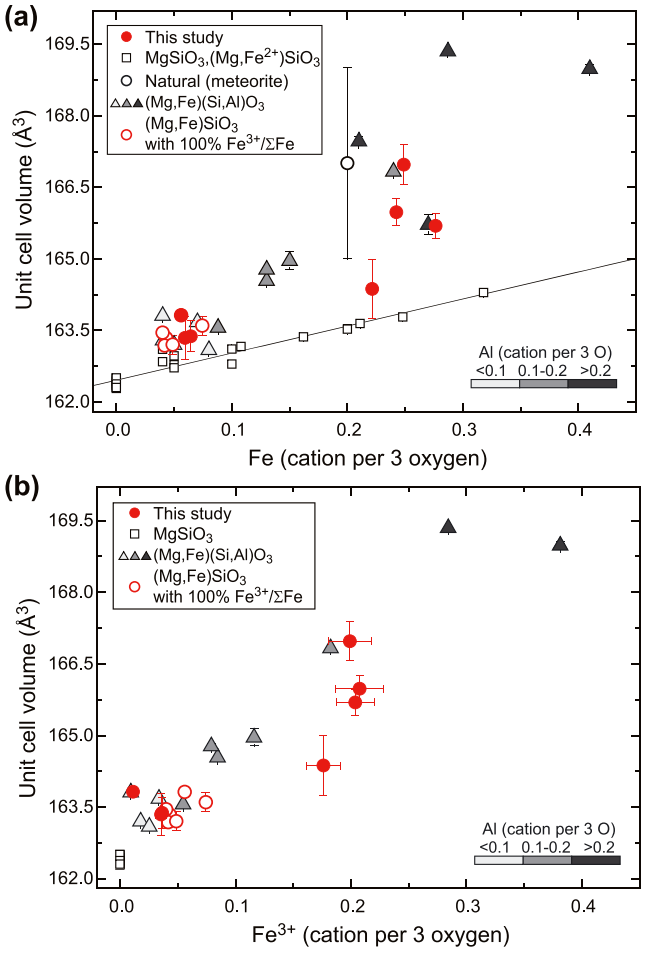

Figure 5. Relationship between the unit cell volume and (a) total iron or (b) Fe^{3+} concentration of bridgmanite. Red filled circles: Al-free bridgmanite of this study; red open circles: Al-free bridgmanite (Hummer & Fei, 2012); open black circle: bridgmanite in the Tenham meteorite (Tschauner et al., 2014); open squares: $(Mg,Fe^{2+})SiO_3$; filled triangles: Al- and Fe-bearing bridgmanite. Literatures for $(Mg,Fe^{2+})SiO_3$ and Al- and Fe-bridgmanite are summarized in Sinmyo, Bykova, et al. (2014). The Al concentrations are indicated by the gray scale.

polaron) is controlled by the impurities and substitution mechanisms in minerals (Yoshino et al., 2016). Similarly, the thermal conductivity is also strongly affected by the substitution of impurities, which serve as an additional source of phonon scattering (Okuda et al., 2017).

4.3. Phase Relations

The results of microprobe analysis are summarized in Table 2 and Figure 6. Although the starting materials were initially prepared with Fe^{3+}/total Fe = 100%, the recovered samples are partially reduced. Based on the results of run #17, the bulk Fe^{3+}/total Fe of the $Mg_{0.95}Fe_{0.10}Si_{0.95}O_3$ and $Mg_{0.75}Fe_{0.50}Si_{0.75}O_3$ bulk compositions is ~0.6 and 0.8, respectively. Although the samples were sealed in chemically inert capsules (Figure 1), the oxygen fugacity may not have been maintained in the sample chamber. Alternatively, oxygen may have been released from minerals by decomposition of iron oxide during the high-pressure and high-temperature experiments, as reported in a recent study (Bykova et al., 2016).

Below 1923 K (Figure 6), bridgmanite and ferropericlase are stable in a pyrolitic bulk composition with less than 3% Fe_2O_3 (Hummer & Fei, 2012; McCammon et al., 1998). Similarly, bridgmanite and stishovite are stable in a basaltic bulk composition with ~3% Fe_2O_3. In both cases, Fe^{3+}-rich iron oxides become stable when the bulk composition is enriched by more than 3% Fe_2O_3 (Figure 6a). Above 1973 K, melt appears over a wide compositional space instead of iron oxides (Figure 6b). This indicates that the solidus of the Fe^{3+}-rich system is significantly lower than that of the Fe^{2+}-dominant bulk composition, which is 2800 K and 26 GPa (Boukare et al., 2015). This result can be partly explained by the lower melting temperature of the iron oxides compared with that of silicate minerals (Myhill et al., 2016).

Since our samples were not buffered in oxygen fugacity (fO_2), the samples may be heterogeneous. Nevertheless, we can constrain the effect of Fe^{3+} on the phase relations under lower mantle conditions, since we have determined the chemical compositions and Fe^{3+}/total Fe ratios of coexisting phases. We note that multi-anvil experiments are widely used without buffering fO_2 to study phase relationships in oxidized/reduced systems (Pamato et al., 2015; Sakamaki et al., 2009).

4.4. Detectability of Fe^{3+}-Rich Oxide and Melt

The Fe^{3+}-rich oxides, such as Fe_4O_5, are stable at relatively low temperatures (<1923 K) in a bulk composition with a high amount of Fe_2O_3 (Figure 6a) (Myhill et al., 2016). Although the elastic parameters of the Fe^{3+}-rich oxide are not well known, seismological observations may not be able to detect such a limited amount of Fe^{3+}-rich oxide. Pioneering works reported that the bulk modulus of Fe^{3+}-rich oxides are moderate; 185.7 GPa for Fe_4O_5 and 173 GPa for Fe_5O_6 (Lavina et al., 2011; Lavina & Meng, 2015). However, Fe^{3+}-rich oxides might induce an electrical conductivity anomaly in the deep mantle because they have an electrical conductivity several orders of magnitude higher than that of silicate (Ovsyannikov et al., 2016). In addition, the melting temperature of materials decreases significantly with increasing Fe^{3+} concentration, as described above. A small degree of melting may be detected by seismology and electromagnetic measurements.

Although the transport of water has long been argued based on knowledge in Fe^{3+}-poor systems (Inoue et al., 2010; Ohtani, 2005), recent studies have shown that the presence of Fe^{3+} can increase the H_2O capacity of minerals under deep mantle conditions (Hu et al., 2016; McCammon et al., 2004; Nishi et al., 2017). The present results suggest that novel Fe^{3+}-rich minerals (e.g., Fe_4O_5) can be stable in stagnant slabs. Although the current study was conducted as an anhydrous system, the Fe^{3+}-rich phase may nevertheless be a

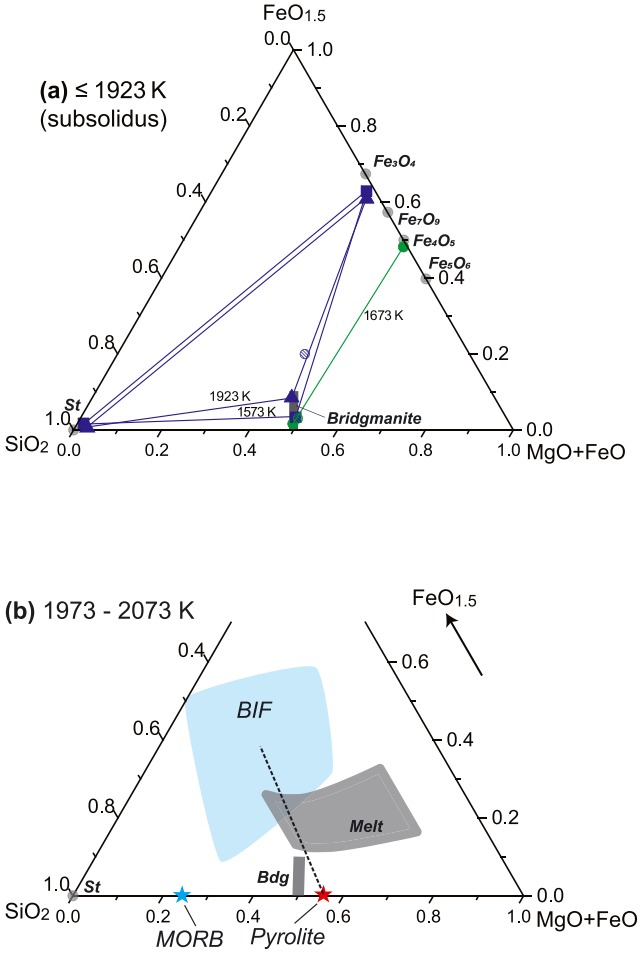

Figure 6. (a) Chemical compositions of the phases coexisting below 1923 K. Results of $Mg_{0.95}Fe_{0.10}Si_{0.95}O_3$ and $Mg_{0.75}Fe_{0.50}Si_{0.75}O_3$ bulk compositions are shown in green and blue symbols, respectively. Hatched circle: starting material; blue square: 1573 K in $Mg_{0.75}Fe_{0.50}Si_{0.75}O_3$; blue triangle: 1923 K in $Mg_{0.75}Fe_{0.50}Si_{0.75}O_3$; green circle: 1673 K in $Mg_{0.95}Fe_{0.10}Si_{0.95}O_3$. The bulk Fe^{3+}/total Fe ratios are assumed to be 0.6 and 0.8 for $Mg_{0.95}Fe_{0.10}Si_{0.95}O_3$ and $Mg_{0.75}Fe_{0.50}Si_{0.75}O_3$ bulk compositions, respectively (see text). (b) Schematic phase diagram of the MgO + $Fe^{2+}O$ − SiO_2 − $Fe^{3+}O_{1.5}$ system at 26 GPa and 1973–2073 K. Chemical compositions of melt were calculated assuming Fe^{3+}/total Fe ratio = 0.5–1. Red star: pyrolite (Trønnes et al., 2018); blue star: Mid-ocean ridge basalt (Trønnes et al., 2018); and light blue region, BIF (Kang & Schmidt, 2017; Spier et al., 2007).

hydrogen host in the deep mantle. In addition, hydrogen can change the defect abundance and arrangement in the crystal structures of lower mantle minerals, and thus, hydrogen may alter conclusions regarding the crystal chemistry and stability of lower mantle phases. However, the phase relations for such compounds remain poorly understood (Bykova et al., 2016), and the role of Fe^{3+} in the transport of water should be investigated further.

4.5. Partitioning of Iron Between Melt and Solid

Although the maximum solubility of total iron (Fe^{2+} + Fe^{3+}) in bridgmanite in our study is much higher than the one measured in reduced bulk compositions, the coexisting liquids are still more iron rich than bridgmanite. The present microprobe analysis shows that the partition coefficient of iron between bridgmanite and melt ($D_{FeO^*}^{Bdg/melt} = X_{FeO^*}^{Bdg}/X_{FeO^*}^{melt}$) ranges from approximately 0.1 to 0.5 depending on the bulk chemistry (Table 2). This is consistent with previous experimental studies (Hirose et al., 2004). In addition, the partitioning coefficient increases with increasing degree of melting (Figure S2), as similar with previous study (Corgne et al., 2005). The partition coefficient of Fe^{3+} between melt and solid was estimated to be 0.1 in the upper mantle based on the chemistry of basalt and peridotite (Canil et al., 1994; Frost & McCammon, 2008). This value is similar to $D_{FeO^*}^{Bdg/melt} = 0.11$ in the $Mg_{0.95}Fe_{0.1}Si_{0.95}O_3$ bulk composition with ~5% melting (run 07). It suggests that the incompatibility of Fe^{3+} is not strongly altered by pressure up to 26 GPa, although it has not been investigated for pressures higher than 26 GPa. Notably, the partitioning coefficient may be also changed by the concentration of Al in the system (Boujibar et al., 2016; Corgne et al., 2005).

The density of partial melt can influence (1) the fate of deep magma (Sakamaki et al., 2006; Sanloup et al., 2013) and (2) the solidification process of the early magma ocean (Labrosse et al., 2007). The latter work proposed the *basal magma ocean* hypothesis based on the enrichment of iron into melt. Although our results support iron enrichment in the melt ($D_{FeO^*}^{Bdg/melt}$ ~ 0.1) at 26 GPa, this value can be altered by spin crossover at higher pressure (Kono et al., 2018; Lin et al., 2013; Murakami et al., 2014; Nomura et al., 2011; Petitgirard et al., 2015; Piet et al., 2016). In the future, the structure and iron spin state in silicate melt should be investigated in situ.

4.6. Redox Melting at the Top of the Lower Mantle?

The present results suggest that oxygen fugacity anomalies in the mantle might dramatically alter the melting and subsolidus phase relations of the lower mantle. As discussed above, the Fe^{3+}-bearing system has a lower solidus temperature than the Fe^{2+}-dominant MgO-FeO-SiO_2 system (Figure 6). The obtained solidus temperature is close to the normal adiabatic geotherm of the lower mantle, which is estimated to be ~2000 K (Katsura et al., 2010) or 1931–2010 K (Stacey & Davis, 2008) at 660 km depth. This suggests that a subducted slab will undergo partial melting if it contains a substantial amount of Fe^{3+} and attains thermal equilibrium with the surrounding mantle. This may be true for the Al-poor system only, because aluminum greatly stabilizes Fe^{3+}-bearing bridgmanite via the Al-Fe^{3+} coupled substitution mechanism (Frost et al., 2004). Indeed, the solidus is reportedly to be ~2500 K at 25 GPa for KLB-1 peridotite (Trønnes & Frost, 2002) and > 2800 K at 25 GPa for Al- and Fe^{3+}-bearing bridgmanite (Andrault et al., 2017). Thus, pyrolite or subducted Al-rich basalt may not melt, even after reaching thermal equilibrium with the surrounding mantle. On the other hand, it is suggested that sedimentary BIFs may be transported into the deep mantle by subduction (Dobson & Brodholt, 2005; Kang & Schmidt, 2017). When the BIF reaches the stagnant slab, small-scale

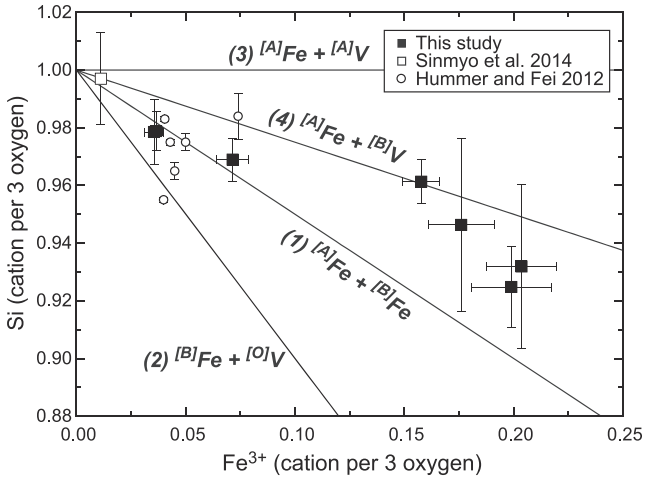

Figure 7. Concentrations of Si and Fe^{3+} in Al-free bridgmanite. The lines indicate four possible substitution mechanisms (see text). Filled squares: this study; open circles: Hummer and Fei (2012); and open square: Sinmyo, Bykova, et al. (2014).

partial melt may be generated from the BIF (Figure 6). Schmandt et al. (2014) reported a low-velocity seismic wave anomaly beneath North America, where the Farallon slab may be in thermal equilibrium with the surrounding mantle (Schmid et al., 2002; Severinghaus et al., 1990). Although such a low-velocity anomaly can be explained by dehydration melting of hydrous ringwoodite (Schmandt et al., 2014), the water content of the transition zone remains debated (Kelbert et al., 2009; Yoshino et al., 2008). The seismic anomaly can alternatively be explained by partial melting induced by Fe^{3+}-rich material subducted below a depth of 660 km, in addition to dehydration melting. While relatively small amount of melt (< 1%) could account for the reduced seismic wave velocity (Schmandt et al., 2014), it is not likely that all seismic anomaly is attributed to the Fe^{3+}-rich melt, since BIF should be a minor thin layer. It is generally accepted that volatile elements, such as hydrogen and carbon, dominantly control the melting temperature (Dasgupta & Hirschmann, 2006; Hirschmann, 2006). However, since these volatile elements are highly incompatible, hydrogen and carbon may be exhausted by partial melting at relatively shallow parts of the subduction zone (Dasgupta & Hirschmann, 2006; Kang & Schmidt, 2017). Indeed, dehydration efficiency during the subduction process is estimated to be as high as >92% (Dixon et al., 2002). On the other hand, as a major element, the bulk oxygen content (i.e., amount of Fe^{3+}) should be as important as the concentration of water and carbon dioxide, although the effect of oxygen content on the melting phase relationships is not yet well understood. In this study, we provide the first results on the effect of bulk oxygen content on melting phase relationships in the lower mantle.

Fe^{3+}-rich melt generated from former BIFs will either ascend or descend from the top of the lower mantle. In general, the fate of silicate melt largely depends on the partitioning of iron between melt and solid (Nomura et al., 2011; Petitgirard et al., 2015). Based on the moderate partition coefficient obtained in this study ($D_{FeO^*}^{Bdg/melt} = 0.1–0.5$), Fe^{3+}-rich melt is likely to be less dense than the surrounding solid at the top of the lower mantle according to recent estimates (Petitgirard et al., 2015), meaning that melt would ascend toward Earth's surface. Although the melting point of Fe^{3+}-rich material is not well known at pressures <25 GPa, the melt should subsequently flow up through the transition zone until it reaches its freezing point. In contrast, residual Fe^{2+}-dominant material will eventually subduct to deeper parts of the lower mantle without further fractionating. This means that the subducted Fe^{3+}-rich component selectively returns from the lower to the upper mantle, which may function as a barrier against oxidizing material at the top of the lower mantle. This process may have a strong effect on the redox state of the mantle and its evolution, similar to redox melting of carbonate-bearing rocks in the upper mantle (Dasgupta & Hirschmann, 2006; Stagno et al., 2013) and the oxygen pump process during core formation (Wood et al., 2006). Modeling of mantle dynamics indicates that oxidized material accumulates in the upper mantle because of the density contrast (Gu et al., 2016). It is important to study the effect of Fe^{3+} on the melting phase relationships at higher pressure for understanding the dynamics of the oxidized material.

5. Conclusions

We have studied the effect of Fe^{3+} on phase relations under lower mantle conditions using a multi-anvil apparatus. Obtained solidus temperature of the Fe^{3+}-bearing system is significantly lower than previously reported ones in the Fe^{3+}-free bulk composition. Strong anomalies in mantle oxygen fugacity affect the melting and subsolidus phase relations of the lower mantle. Further studies are required for better understanding the dynamics of the oxidized materials in deep mantle.

Acknowledgments
R. S. was supported by a Research Fellowship for Postdoctoral Researchers awarded by the Alexander von Humboldt Foundation. S. P. was financed by a grant from DFG (PE 2334/1-1). The FEI© Scios Dual Beam focused ion beam at the Bayerisches Geoinstitut, University of Bayreuth, was financed through DFG grant INST 91/315-1 FUGG. We used program EELSA developed by C. Prescher in the analysis of ELNES data. Data for Figures 5 are all shown in Tables 1 and uploaded to Figshare https://figshare.com/articles/JGR_2019_Tables/9918041. We thank two anonymous reviewers for fruitful comments.

References

Andrault, D., & Bolfan-Casanova, N. (2001). High-pressure phase transformations in the $MgFe_2O_4$ and Fe_2O_3-$MgSiO_3$ systems. *Physics and Chemistry of Minerals*, *28*(3), 211–217. https://doi.org/10.1007/s002690000149

Andrault, D., Bolfan-Casanova, N., Bouhifd, M. A., Boujibar, A., Garbarino, G., Manthilake, G., et al. (2017). Toward a coherent model for the melting behavior of the deep Earth's mantle. *Physics of the Earth and Planetary Interiors*, *265*, 67–81. https://doi.org/10.1016/j.pepi.2017.02.009

Bolfan-Casanova, N., Keppler, H., & Rubie, D. C. (2000). Water partitioning between nominally anhydrous minerals in the MgO-SiO_2-H_2O system up to 24 GPa: Implications for the distribution of water in the Earth's mantle. *Earth and Planetary Science Letters*, *182*(3-4), 209–221. https://doi.org/10.1016/s0012-821x(00)00244-2

Bolfan-Casanova, N., Keppler, H., & Rubie, D. C. (2003). Water partitioning at 660 km depth and evidence for very low water solubility in magnesium silicate perovskite. *Geophysical Research Letters*, *30*(17), n/a. https://doi.org/10.1029/2003GL017182

Boujibar, A., Bolfan-Casanova, N., Andrault, D., Bouhifd, M. A., & Trcera, N. (2016). Incorporation of Fe^{2+} and Fe^{3+} in bridgmanite during magma ocean crystallization. *American Mineralogist*, *101*(7), 1560–1570. https://doi.org/10.2138/am-2016-5561

Boukare, C. E., Ricard, Y., & Fiquet, G. (2015). Thermodynamics of the MgO-FeO-SiO_2 system up to 140 GPa: Application to the crystallization of Earth's magma ocean. *Journal of Geophysical Research: Solid Earth*, *120*, 6085–6101. https://doi.org/10.1002/2015jb011929

Bykova, E., Dubrovinsky, L., Dubrovinskaia, N., Bykov, M., McCammon, C., Ovsyannikov, S. V., et al. (2016). Structural complexity of simple Fe_2O_3 at high pressures and temperatures. *Nature Communications*, *7*, 10661. https://doi.org/10.1038/ncomms10661

Canil, D., O'Neill, H. S. C., Pearson, D., Rudnick, R., McDonough, W., & Carswell, D. (1994). Ferric iron in peridotites and mantle oxidation states. *Earth and Planetary Science Letters*, *123*(1-3), 205–220. https://doi.org/10.1016/0012-821X(94)90268-2

Corgne, A., Liebske, C., Wood, B. J., Rubie, D. C., & Frost, D. J. (2005). Silicate perovskite-melt partitioning of trace elements and geochemical signature of a deep perovskitic reservoir. *Geochimica et Cosmochimica Acta*, *69*(2), 485–496. https://doi.org/10.1016/j.gca.2004.06.041

Dasgupta, R., & Hirschmann, M. M. (2006). Melting in the Earth's deep upper mantle caused by carbon dioxide. *Nature*, *440*(7084), 659–662. https://doi.org/10.1038/nature04612

Dixon, J. E., Leist, L., Langmuir, C., & Schilling, J.-G. (2002). Recycled dehydrated lithosphere observed in plume-influenced mid-ocean-ridge basalt. *Nature*, *420*(6914), 385–389. https://doi.org/10.1038/nature01215

Dobson, D. P., & Brodholt, J. P. (2005). Subducted banded iron formations as a source of ultralow-velocity zones at the core-mantle boundary. *Nature*, *434*(7031), 367–371. https://doi.org/10.1038/nature03385

Fei, Y., Mao, H. K., & Mysen, B. O. (1991). Experimental determination of element partitioning and calculation of phase relations in the MgO-FeO-SiO_2 system at high pressure and high temperature. *Journal of Geophysical Research*, *96*(B2), 2157–2169. https://doi.org/10.1029/90jb02164

Fei, Y., Van Orman, J., Li, J., van Westrenen, W., Sanloup, C., Minarik, W., et al. (2004). Experimentally determined postspinel transformation boundary in Mg_2SiO_4 using MgO as an internal pressure standard and its geophysical implications. *Journal of Geophysical Research-Solid Earth*, *109*(B2), B02305. https://doi.org/10.1029/2003jb002562

Freitas, D., Manthilake, G., Schiavi, F., Chantel, J., Bolfan-Casanova, N., Bouhifd, M. A., & Andrault, D. (2017). Experimental evidence supporting a global melt layer at the base of the Earth's upper mantle. *Nature Communications*, *8*(1), 2186. https://doi.org/10.1038/s41467-017-02275-9

Frost, D. J., Liebske, C., Langenhorst, F., McCammon, C. A., Tronnes, R. G., & Rubie, D. C. (2004). Experimental evidence for the existence of iron-rich metal in the Earth's lower mantle. *Nature*, *428*(6981), 409–412. https://doi.org/10.1038/nature02413

Frost, D. J., & McCammon, C. A. (2008). The redox state of Earth's mantle. *Annual Review of Earth and Planetary Sciences*, *36*(1), 389–420. https://doi.org/10.1146/annurev.earth.36.031207.124322

Frost, D. J., & McCammon, C. A. (2009). The effect of oxygen fugacity on the olivine to wadsleyite transformation: Implications for remote sensing of mantle redox state at the 410 km seismic discontinuity. *American Mineralogist*, *94*(7), 872–882. https://doi.org/10.2138/am.2009.3094

Frost, D. J., & Myhill, R. (2016). Chemistry of the lower mantle. *Deep Earth: Physics and Chemistry of the lower mantle and core, Geophysical Monograph*, *217*, 225–240.

Gu, T. T., Li, M. M., McCammon, C., & Lee, K. K. M. (2016). Redox-induced lower mantle density contrast and effect on mantle structure and primitive oxygen. *Nature Geoscience*, *9*(9), 723–727. https://doi.org/10.1038/ngeo2772

Hirose, K., Shimizu, N., van Westrenen, W., & Fei, Y. (2004). Trace element partitioning in Earth's lower mantle and implications for geochemical consequences of partial melting at the core–mantle boundary. *Physics of the Earth and Planetary Interiors*, *146*(1-2), 249–260. https://doi.org/10.1016/j.pepi.2002.11.001

Hirschmann, M. M. (2006). Water, melting, and the deep Earth H_2O cycle. *Annual Review of Earth and Planetary Sciences*, *34*(1), 629–653. https://doi.org/10.1146/annurev.earth.34.031405.125211

Hu, Q., Kim, D. Y., Yang, W., Yang, L., Meng, Y., Zhang, L., & Mao, H. K. (2016). FeO_2 and FeOOH under deep lower-mantle conditions and Earth's oxygen-hydrogen cycles. *Nature*, *534*(7606), 241–244. https://doi.org/10.1038/nature18018

Hummer, D. R., & Fei, Y. (2012). Synthesis and crystal chemistry of Fe^{3+}-bearing $(Mg,Fe^{3+})(Si,Fe^{3+})O_3$ perovskite. *American Mineralogist*, *97*(11-12), 1915–1921. https://doi.org/10.2138/am.2012.4144

Inoue, T., Wada, T., Sasaki, R., & Yurimoto, H. (2010). Water partitioning in the Earth's mantle. *Physics of the Earth and Planetary Interiors*, *183*(1-2), 245–251. https://doi.org/10.1016/j.pepi.2010.08.003

Ishii, T., Huang, R., Fei, H., Koemets, I., Liu, Z., Maeda, F., et al. (2018). Complete agreement of the post-spinel transition with the 660-km seismic discontinuity. *Scientific Reports*, *8*(1), 6358. https://doi.org/10.1038/s41598-018-24832-y

Ishii, T., Uenver-Thiele, L., Woodland, A. B., Alig, E., & Ballaran, T. B. (2018). Synthesis and crystal structure of Mg-bearing Fe_9O_{11}: New insight in the complexity of Fe-Mg oxides at conditions of the deep upper mantle. *American Mineralogist*, *103*(11), 1873–1876.

Ito, E., Kubo, A., Katsura, T., & Walter, M. J. (2004). Melting experiments of mantle materials under lower mantle conditions with implications for magma ocean differentiation. *Physics of the Earth and Planetary Interiors*, *143-144*, 397–406. https://doi.org/10.1016/j.pepi.2003.09.016

Ito, E., & Takahashi, E. (1989). Postspinel transformations in the system Mg_2SiO_4-Fe_2SiO_4 and some geophysical implications. *Journal of Geophysical Research*, *94*(B8), 10637–10646. https://doi.org/10.1029/JB094iB08p10637

Kagi, H., Zedgenizov, D. A., Ohfuji, H., & Ishibashi, H. (2016). Micro-and nano-inclusions in a superdeep diamond from São Luiz, Brazil. *Geochemistry International*, *54*(10), 834–838. https://doi.org/10.1134/S0016702916100062

Kaminsky, F. V., Ryabchikov, I. D., McCammon, C. A., Longo, M., Abakumov, A. M., Turner, S., & Heidari, H. (2015). Oxidation potential in the Earth's lower mantle as recorded by ferropericlase inclusions in diamond. *Earth and Planetary Science Letters*, *417*, 49–56. https://doi.org/10.1016/j.epsl.2015.02.029

Kang, N., & Schmidt, M. W. (2017). The melting of subducted banded iron formations. *Earth and Planetary Science Letters*, *476*, 165–178. https://doi.org/10.1016/j.epsl.2017.07.040

Katsura, T., Yoneda, A., Yamazaki, D., Yoshino, T., & Ito, E. (2010). Adiabatic temperature profile in the mantle. *Physics of the Earth and Planetary Interiors*, *183*(1-2), 212–218. https://doi.org/10.1016/j.pepi.2010.07.001

Kelbert, A., Schultz, A., & Egbert, G. (2009). Global electromagnetic induction constraints on transition-zone water content variations. *Nature*, *460*(7258), 1003–1006. https://doi.org/10.1038/nature08257

Keppler, H., & Frost, D. J. (2005). Introduction to minerals under extreme conditions. In R. Miletich (Ed.), *Mineral Behaviour at Extreme Conditions* (Chap. 1, pp. 1-30, Vol. 7). Budapest: Eötvös Univ. Press. https://doi.org/10.1180/EMU-notes.7.1

Kiseeva, E. S., Vasiukov, D. M., Wood, B. J., McCammon, C., Stachel, T., Bykov, M., et al. (2018). Oxidized iron in garnets from the mantle transition zone. *Nature Geoscience*, *11*(2), 144–147. https://doi.org/10.1038/s41561-017-0055-7

Kono, Y., Shibazaki, Y., Kenney-Benson, C., Wang, Y., & Shen, G. (2018). Pressure-induced structural change in $MgSiO_3$ glass at pressures near the Earth's core–mantle boundary. *Proceedings of the National Academy of Sciences of the United States of America*, *115*(8), 1742–1747. https://doi.org/10.1073/pnas.1716748115

Kröger, F., & Vink, H. (1956). Relations between the concentrations of imperfections in crystalline solids. In *Solid State Physics* (Vol. *3*, pp. 307-435): Elsevier.

Kurnosov, A., Marquardt, H., Frost, D., Ballaran, T. B., & Ziberna, L. (2017). Evidence for a Fe^{3+}-rich pyrolitic lower mantle from (Al, Fe)-bearing bridgmanite elasticity data. *Nature*, *543*(7646), 543–546. https://doi.org/10.1038/nature21390

Labrosse, S., Hernlund, J. W., & Coltice, N. (2007). A crystallizing dense magma ocean at the base of the Earth's mantle. *Nature*, *450*(7171), 866–869. https://doi.org/10.1038/nature06355

Lauterbach, S., McCammon, C. A., van Aken, P., Langenhorst, F., & Seifert, F. (2000). Mössbauer and ELNES spectroscopy of (Mg,Fe)(Si, Al)O_3 perovskite: A highly oxidised component of the lower mantle. *Contributions to Mineralogy and Petrology*, *138*(1), 17–26. https://doi.org/10.1007/pl00007658

Lavina, B., Dera, P., Kim, E., Meng, Y., Downs, R. T., Weck, P. F., et al. (2011). Discovery of the recoverable high-pressure iron oxide Fe_4O_5. *Proceedings of the National Academy of Sciences of the United States of America*, *108*(42), 17281–17285. https://doi.org/10.1073/pnas.1107573108

Lavina, B., & Meng, Y. (2015). Unraveling the complexity of iron oxides at high pressure and temperature: Synthesis of Fe_5O_6. *Science Advances*, *1*(5), e1400260. https://doi.org/10.1126/sciadv.1400260

Liebske, C., & Frost, D. J. (2012). Melting phase relations in the MgO-$MgSiO_3$ system between 16 and 26 GPa: Implications for melting in Earth's deep interior. *Earth and Planetary Science Letters*, *345-348*, 159–170. https://doi.org/10.1016/j.epsl.2012.06.038

Lin, J. F., Speziale, S., Mao, Z., & Marquardt, H. (2013). Effects of the electronic spin transitions of iron in lower mantle minerals: Implications for deep mantle geophysics and geochemistry. *Reviews of Geophysics*, *51*, 244–275. https://doi.org/10.1002/rog.20010

Litasov, K. D., Shatskiy, A., & Ohtani, E. (2014). Melting and subsolidus phase relations in peridotite and eclogite systems with reduced COH fluid at 3-16 GPa. *Earth and Planetary Science Letters*, *391*, 87–99. https://doi.org/10.1016/j.epsl.2014.01.033

Liu, Z., Akaogi, M., & Katsura, T. (2019). Increase of the oxygen vacancy component in bridgmanite with temperature. *Earth and Planetary Science Letters*, *505*, 141–151. https://doi.org/10.1016/j.epsl.2018.10.014

Liu, Z., Park, J., & Karato, S. I. (2018). Seismic evidence for water transport out of the mantle transition zone beneath the European Alps. *Earth and Planetary Science Letters*, *482*, 93–104. https://doi.org/10.1016/j.epsl.2017.10.054

Longo, M., McCammon, C. A., & Jacobsen, S. D. (2011). Microanalysis of the iron oxidation state in (Mg,Fe)O and application to the study of microscale processes. *Contributions to Mineralogy and Petrology*, *162*(6), 1249–1257. https://doi.org/10.1007/s00410-011-0649-9

McCammon, C., Peyronneau, J., & Poirier, J. P. (1998). Low ferric iron content of (Mg,Fe)O at high pressures and temperatures. *Geophysical Research Letters*, *25*(10), 1589–1592. https://doi.org/10.1029/98gl01178

McCammon, C. A., Frost, D. J., Smyth, J. R., Laustsen, H. M. S., Kawamoto, T., Ross, N. L., & van Aken, P. A. (2004). Oxidation state of iron in hydrous mantle phases: implications for subduction and mantle oxygen fugacity. *Physics of the Earth and Planetary Interiors*, *143-144*, 157–169. https://doi.org/10.1016/j.pepi.2003.08.009

Merlini, M., Hanfland, M., Salamat, A., Petitgirard, S., & Muller, H. (2015). The crystal structures of $Mg_2Fe_2C_4O_{13}$, with tetrahedrally coordinated carbon, and $Fe_{13}O_{19}$, synthesized at deep mantle conditions. *American Mineralogist*, *100*(8-9), 2001–2004. https://doi.org/10.2138/am-2015-5369

Murakami, M., Goncharov, A. F., Hirao, N., Masuda, R., Mitsui, T., Thomas, S. M., & Bina, C. R. (2014). High-pressure radiative conductivity of dense silicate glasses with potential implications for dark magmas. *Nature Communications*, *5*, 5428. https://doi.org/10.1038/ncomms6428

Myhill, R., Ojwang, D. O., Ziberna, L., Frost, D. J., Ballaran, T. B., & Miyajima, N. (2016). On the *P-T-f*O_2 stability of Fe_4O_5, Fe_5O_6 and Fe_4O_5-rich solid solutions. *Contributions to Mineralogy and Petrology*, *171*, 51. https://doi.org/10.1007/s00410-016-1258-4

Nakajima, Y., Frost, D. J., & Rubie, D. C. (2012). Ferrous iron partitioning between magnesium silicate perovskite and ferropericlase and the composition of perovskite in the Earth's lower mantle. *Journal of Geophysical Research-Solid Earth*, *117*(B8), B08201. https://doi.org/10.1029/2012jb009151

Nishi, M., Kuwayama, Y., Tsuchiya, J., & Tsuchiya, T. (2017). The pyrite-type high-pressure form of FeOOH. *Nature*, *547*(7662), 205–208. https://doi.org/10.1038/nature22823

Nomura, R., Ozawa, H., Tateno, S., Hirose, K., Hernlund, J., Muto, S., et al. (2011). Spin crossover and iron-rich silicate melt in the Earth's deep mantle. *Nature*, *473*(7346), 199–202. https://doi.org/10.1038/nature09940

Ohtani, E. (2005). Water in the mantle. *Elements*, *1*(1), 25–30. https://doi.org/10.2113/gselements.1.1.25

Okuda, Y., Ohta, K., Yagi, T., Sinmyo, R., Wakamatsu, T., Hirose, K., & Ohishi, Y. (2017). The effect of iron and aluminum incorporation on lattice thermal conductivity of bridgmanite at the Earth's lower mantle. *Earth and Planetary Science Letters*, *474*, 25–31. https://doi.org/10.1016/j.epsl.2017.06.022

Ovsyannikov, S. V., Bykov, M., Bykova, E., Kozlenko, D. P., Tsirlin, A. A., Karkin, A. E., et al. (2016). Charge-ordering transition in iron oxide Fe_4O_5 involving competing dimer and trimer formation. *Nature Chemistry*, *8*(5), 501–508. https://doi.org/10.1038/nchem.2478

Pamato, M. G., Myhill, R., Ballaran, T. B., Frost, D. J., Heidelbach, F., & Miyajima, N. (2015). Lower-mantle water reservoir implied by the extreme stability of a hydrous aluminosilicate. *Nature Geoscience*, *8*(1), 75–79. https://doi.org/10.1038/ngeo2306

Pearson, D. G., Brenker, F. E., Nestola, F., McNeill, J., Nasdala, L., Hutchison, M. T., et al. (2014). Hydrous mantle transition zone indicated by ringwoodite included within diamond. *Nature*, *507*(7491), 221–224. https://doi.org/10.1038/nature13080

Petitgirard, S., Malfait, W. J., Sinmyo, R., Kupenko, I., Hennet, L., Harries, D., et al. (2015). Fate of $MgSiO_3$ melts at core-mantle boundary conditions. *Proceedings of the National Academy of Sciences of the United States of America*, *112*(46), 14186–14190. https://doi.org/10.1073/pnas.1512386112

Piet, H., Badro, J., Nabiei, F., Dennenwaldt, T., Shim, S. H., Cantoni, M., et al. (2016). Spin and valence dependence of iron partitioning in Earth's deep mantle. *Proceedings of the National Academy of Sciences of the United States of America*, *113*(40), 11127–11130. https://doi.org/10.1073/pnas.1605290113

Prescher, C., McCammon, C., & Dubrovinsky, L. (2012). MossA: A program for analyzing energy-domain Mössbauer spectra from conventional and synchrotron sources. *Journal of Applied Crystallography*, *45*(2), 329–331. https://doi.org/10.1107/s0021889812004979

Rohrbach, A., Ballhaus, C., Golla–Schindler, U., Ulmer, P., Kamenetsky, V. S., & Kuzmin, D. V. (2007). Metal saturation in the upper mantle. *Nature*, *449*(7161), 456–458. https://doi.org/10.1038/nature06183

Rubie, D. C., Karato, S., Yan, H., & Oneill, H. S. C. (1993). Low differential stress and controlled chemical environment in multianvil high-pressure experiments. *Physics and Chemistry of Minerals*, *20*(5), 315–322.

Sakamaki, K., Takahashi, E., Nakajima, Y., Nishihara, Y., Funakoshi, K., Suzuki, T., & Fukai, Y. (2009). Melting phase relation of FeHx up to 20 GPa: Implication for the temperature of the Earth's core. *Physics of the Earth and Planetary Interiors*, *174*(1-4), 192–201. https://doi.org/10.1016/j.pepi.2008.05.017

Sakamaki, T., Suzuki, A., & Ohtani, E. (2006). Stability of hydrous melt at the base of the Earth's upper mantle. *Nature*, *439*(7073), 192–194. https://doi.org/10.1038/nature04352

Sanloup, C., Drewitt, J. W., Konôpková, Z., Dalladay-Simpson, P., Morton, D. M., Rai, N., et al. (2013). Structural change in molten basalt at deep mantle conditions. *Nature*, *503*(7474), 104–107. https://doi.org/10.1038/nature12668

Schmandt, B., Jacobsen, S. D., Becker, T. W., Liu, Z., & Dueker, K. G. (2014). Dehydration melting at the top of the lower mantle. *Science*, *344*(6189), 1265–1268. https://doi.org/10.1126/science.1253358

Schmid, C., Goes, S., Van der Lee, S., & Giardini, D. (2002). Fate of the Cenozoic Farallon slab from a comparison of kinematic thermal modeling with tomographic images. *Earth and Planetary Science Letters*, *204*(1-2), 17–32. https://doi.org/10.1016/S0012-821X(02)00985-8

Severinghaus, J., & Atwater, T. (1990). *Cenozoic geometry and thermal state of the subducting slabs beneath western North America* (Vol. 176, pp. 1–22). Basin and range extensional tectonics near the latitude of Las Vegas, Nevada: Geological Society of America Memoir. https://doi.org/10.1130/MEM176-p1

Shim, S. H., Grocholski, B., Ye, Y., Alp, E. E., Xu, S., Morgan, D., et al. (2017). Stability of ferrous-iron-rich bridgmanite under reducing midmantle conditions. *Proceedings of the National Academy of Sciences of the United States of America*, *114*(25), 6468–6473. https://doi.org/10.1073/pnas.1614036114

Siegel, R. W. (1978). Vacancy concentrations in metals. *Journal of Nuclear Materials*, *69*, 117–146.

Sinmyo, R., Bykova, E., McCammon, C., Kupenko, I., Potapkin, V., & Dubrovinsky, L. (2014). Crystal chemistry of Fe^{3+}-bearing (Mg, Fe)SiO_3 perovskite: a single-crystal X-ray diffraction study. *Physics and Chemistry of Minerals*, *41*(6), 409–417. https://doi.org/10.1007/s00269-013-0639-8

Sinmyo, R., Bykova, E., Ovsyannikov, S. V., McCammon, C., Kupenko, I., Ismailova, L., & Dubrovinsky, L. (2016). Discovery of Fe_7O_9: A new iron oxide with a complex monoclinic structure. *Scientific Reports*, *6*(1), 32852. https://doi.org/10.1038/srep32852

Sinmyo, R., McCammon, C., & Dubrovinsky, L. (2017). The spin state of Fe^{3+} in lower mantle bridgmanite. *American Mineralogist*, *102*(6), 1263–1269. https://doi.org/10.2138/am-2017-5917

Sinmyo, R., Pesce, G., Greenberg, E., McCammon, C., & Dubrovinsky, L. (2014). Lower mantle electrical conductivity based on measurements of Al, Fe-bearing perovskite under lower mantle conditions. *Earth and Planetary Science Letters*, *393*, 165–172. https://doi.org/10.1016/j.epsl.2014.02.049

Smith, E. M., Shirey, S. B., Nestola, F., Bullock, E. S., Wang, J., Richardson, S. H., & Wang, W. (2016). Large gem diamonds from metallic liquid in Earth's deep mantle. *Science*, *354*(6318), 1403–1405. https://doi.org/10.1126/science.aal1303

Spier, C. A., de Oliveira, S. M., Sial, A. N., & Rios, F. J. (2007). Geochemistry and genesis of the banded iron formations of the Cauê Formation, Quadrilátero Ferrífero, Minas Gerais, Brazil. *Precambrian Research*, *152*(3-4), 170–206. https://doi.org/10.1016/j.precamres.2006.10.003

Stacey, F. D., & Davis, P. M. (2008). *Physics of the Earth* (4th ed.). Cambridge: Cambridge University Press. https://doi.org/10.1017/CBO9780511812910

Stagno, V., Ojwang, D. O., McCammon, C. A., & Frost, D. J. (2013). The oxidation state of the mantle and the extraction of carbon from Earth's interior. *Nature*, *493*(7430), 84–88. https://doi.org/10.1038/nature11679

Trønnes, R. G., Baron, M. A., Eigenmann, K. R., Guren, M. G., Heyn, B. H., Løken, A., & Mohn, C. E. (2018). Core formation, mantle differentiation and core-mantle interaction within Earth and the terrestrial planets. *Tectonophysics*, *760*, 165–198.

Trønnes, R. G., & Frost, D. J. (2002). Peridotite melting and mineral-melt partitioning of major and minor elements at 22-24.5 GPa. *Earth and Planetary Science Letters*, *197*(1-2), 117–131. https://doi.org/10.1016/S0012-821X(02)00466-1

Tschauner, O., Huang, S., Greenberg, E., Prakapenka, V. B., Ma, C., Rossman, G. R., et al. (2018). Ice-VII inclusions in diamonds: Evidence for aqueous fluid in Earth's deep mantle. *Science*, *359*(6380), 1136–1139. https://doi.org/10.1126/science.aao3030

Tschauner, O., Ma, C., Beckett, J. R., Prescher, C., Prakapenka, V. B., & Rossman, G. R. (2014). Discovery of bridgmanite, the most abundant mineral in Earth, in a shocked meteorite. *Science*, *346*(6213), 1100–1102. https://doi.org/10.1126/science.1259369

Uenver-Thiele, L., Woodland, A. B., Ballaran, T. B., Miyajima, N., & Frost, D. J. (2017). Phase relations of $MgFe_2O_4$ at conditions of the deep upper mantle and transition zone. *American Mineralogist*, *102*(3), 632–642. https://doi.org/10.2138/am-2017-5871

van Aken, P. A., Liebscher, B., & Styrsa, V. J. (1998). Quantitative determination of iron oxidation states in minerals using Fe $L_{2,3}$-edge electron energy-loss near-edge structure spectroscopy. *Physics and Chemistry of Minerals*, *25*(5), 323–327. https://doi.org/10.1007/s002690050122

Wirth, R., Dobrzhinetskaya, L., Harte, B., Schreiber, A., & Green, H. (2014). High-Fe (Mg, Fe) O inclusion in diamond apparently from the lowermost mantle. *Earth and Planetary Science Letters*, *404*, 365–375. https://doi.org/10.1016/j.epsl.2014.08.010

Wood, B. J., Walter, M. J., & Wade, J. (2006). Accretion of the Earth and segregation of its core. *Nature*, *441*(7095), 825–833. https://doi.org/10.1038/nature04763

Yoshino, T., Kamada, S., Zhao, C., Ohtani, E., & Hirao, N. (2016). Electrical conductivity model of Al-bearing bridgmanite with implications for the electrical structure of the Earth's lower mantle. *Earth and Planetary Science Letters*, *434*, 208–219. https://doi.org/10.1016/j.epsl.2015.11.032

Yoshino, T., Manthilake, G., Matsuzaki, T., & Katsura, T. (2008). Dry mantle transition zone inferred from the conductivity of wadsleyite and ringwoodite. *Nature*, *451*(7176), 326–329. https://doi.org/10.1038/nature06427